

Stability Analysis of Microgrid with Passive, Active, and Dynamic Load

K. Matharani*, H. Jariwala

Department of Electrical Engineering, SVNIT, Surat, India

Abstract— The autonomous microgrid can incur a stability issue due to the low inertia offered by power electronics-based distributed generating sources of the microgrid. Due to the fast dynamics of inverters and the intermittent nature of renewables, the first phase of abrupt load change might not be shared evenly by DGs, and the system's stability deteriorates substantially. Hence the stability of the microgrid can greatly influenced by the load dynamics because of the inertialess generating sources. This paper presents a stability analysis of microgrid considering passive, active, and dynamic loads fed by inverter-based DGs. The small-signal analysis demonstrates the effect of inverter parameters and load factors. The dominance of states in oscillatory mode is examined by participation analysis. The results show that passive load does not introduce low-frequency mode, whereas rectifier interfaced active load (RIAL) introduces low-frequency mode due to DC voltage controller. The induction motor (IM) load introduces less damped eigenvalues in the microgrid and profoundly affects the real power-sharing of the system. The time-domain results verify the results obtained through eigenvalue analysis.

Keywords—Microgrid, Distributed generation units, Rectifier interfaced active load, Passive load, Induction motor load.

NOMENCLATURE

ω	angular frequency of common reference frame	r_f, r_c	internal resistance of LC filter and coupling inductor
F	feed-forward gain	r_s, r_r	resistance of stator and rotor windings
$i_{d,AL}^*, i_{q,AL}^*$	d and q axis inductor reference currents of RIAL	R_{linei}, L_{linei}	resistance and inductance of line
$i_{d,AL}^*, i_{q,AL}^*$	d and q axis inductor reference currents	R_{loadi}, L_{loadi}	resistance and inductance of i^{th} RL load
i_{conv}, i_{dc}	output current of AC to DC converter and load current	T_e, T_L	electromagnetic torque and load torque of IM
i_{Dr}, i_{Qr}	D and Q axis rotor currents of IM	v_{dc}^*, v_{dc}	reference voltage and actual voltage across dc load
i_{Ds}, i_{Qs}	D and Q axis stator currents of IM	v_{id}^*, v_{iq}^*	d and q axis inverter reference voltages
i_{gd}, i_{gq}	d and q axis input current of RIAL	v_{od}^*, v_{oq}^*	d and q axis output reference voltages
i_{lineDi}, i_{lineQi}	line currents in DQ reference frame	v_n	nominal set point voltage
i_{loaDi}, i_{loaQi}	load currents in DQ reference frame	v_{bD}, v_{bQ}	D and Q axis bus voltages in common reference frame
i_{od}, i_{oq}	d and q axis output current of DG	v_{bd}, v_{bq}	d and q axis bus voltages in the inverter reference frame
J	total motor and load inertia	v_{Dr}, v_{Qr}	D and Q axis rotor voltages of IM
k_{pc}, k_{ic}	proportional and integral gain of current controller	v_{Ds}, v_{Qs}	D and Q axis stator voltages of IM
$k_{pv,AL}, k_{iv,AL}$	proportional and integral gain of AC current controller of RIAL	$v_{od,AL}, v_{oq,AL}$	d and q axis voltage across capacitor of RIAL
k_{pv}, k_{iv}	proportional and integral gain of voltage controller	v_{od}, v_{oq}	d and q axis output voltage of DG
L_c	inductance of coupling inductor	δ_i	angle between i^{th} inverter's reference frame and common reference frame
L_f, C_f	inductance and capacitance of LC filter	\emptyset_d, \emptyset_q	state variables of voltage controller
$L_{f,AL}, C_{f,AL}$	inductance and capacitance of LC filter of RIAL	\emptyset_{AL}	state variable of DC voltage controller in RIAL
L_{SS}, L_{rr}, L_m	inductance of stator and rotor windings, mutual inductance of IM	\emptyset_{ki}	k^{th} element in left eigenvector for i^{th} eigenvalue
m_p, n_q	real power and reactive power droop gain	γ_d, γ_q	state variables of current controller
P_{IM}	number of poles	$\gamma_{d,AL}, \gamma_{q,AL}$	State variables of active load current controller
P_{in}, P	instantaneous and average real power of DG	ω_s	angular synchronous speed
P_{ki}	participation element of k^{th} state variable in i^{th} eigenvalue	ω_{cf}	cut-off frequency of low pass filter
Q_{in}, Q	instantaneous and average reactive power of DG	ω_n	nominal set point frequency

1. INTRODUCTION

A microgrid is a part of a modern energy system that comprises distributed generation (DG) units, energy storage units, and loads. The DGs in microgrid can be photovoltaic cells (PV), fuel cells (FC), and microturbine (MT) [1–3]. The PVs and FCs generate DC power while MTs and wind farm generates variable frequency ac power. All DGs are interconnected in the microgrid using power electronics converters. Since power electronics-based converters

Received: 02 Mar. 2022

Revised: 06 Jul. 2022

Accepted: 26 Jul. 2022

*Corresponding author:

E-mail: kinbaheti@gmail.com (K. Matharani)

DOI: 10.22098/JOAPE.2024.10445.1741

Research Paper

©2024 University of Mohaghegh Ardabili. All rights reserved

offer high efficiency and operational flexibility, they are commonly employed in power conversion and control [4]. The microgrid's ability to operate in an autonomous and grid-tied mode offers immense reliability, expandability, and generation of high-quality green energy [5–11]. In grid-connected mode, the microgrid supplies active and reactive electricity to the main grid as an extra energy source. In this mode, the microgrid's frequency and voltage parameters are maintained because of the primary grid. In islanded or autonomous mode, besides supplying power to the load, it has to maintain voltage and frequency within permissible limits [12]. The stability of a microgrid is essential for its reliable operation. The nature of generating sources, operating modes, control strategies, the response speed of DG, and distance from source to load are different in a microgrid as compared to a traditional grid. The low inertia of DGs in a microgrid operating in islanded mode makes the system operation complicated when the load and network parameters suddenly change. Therefore, it is essential to account for the load as well as dynamics of the distribution network while performing a stability analysis of a microgrid.

The transient stability of AC and DC microgrids is investigated in [13] using a prosumer-based approach. The modified converter control strategy is applied to see the response of the microgrid during a temporary fault, permanent fault, and significant variations in load. The frequency stability of the microgrid is investigated with a novel linear controller applied to the diesel generator's speed governor system in [4]. In [14], the voltage stability of a microgrid is analyzed using a modified voltage stability index for a two-tier load model. The optimum size and best allocation of DGs are obtained by using the imperialist competition algorithm to improve the voltage stability and reduce losses. The transient stability of an autonomous microgrid using a novel energy-based approach is evaluated in [15]. The dissipativity and neutral connections of the microgrid are investigated using the Takagi-Sugeno based multimodal [15]. In [16], the review of various approaches for the transient stability and small-signal analysis of microgrids is presented. Additionally, the response of DGs to large disturbances and the fault current contributions of different DGs using various control strategies are investigated and discussed.

The small-signal stability is the analysis of the behavior of the system after small disturbances. The state-space modeling technique has been appreciably utilized in literature to develop non-linear or linearized models that are useful in accessing the dynamic response and stability of the microgrid [17–20]. In [21], the stability of a microgrid is analyzed with angle droop and frequency control considering passive load. The non-linear load is also taken into account, but it only gives an idea of the power quality issues of microgrids. The small-signal stability of a microgrid with RL load is analyzed using perturbation theory in [22] for various values of droop gains, load resistance, and load reactance. In [23], the authors have developed a complete state-space model of the microgrid and analyzed the system considering passive load. The damping resistor can be used to reduce oscillations along with a phase-locked loop (PLL) by considering the effect of passive load in a microgrid [24]. The state-space model of microgrid consisting of different architecture of wind power (WP), PV, and a diesel generator is developed and explored in [25]. Time-domain analysis of different source (WP, MT, FC, and PV) based systems with different control strategies are studied in [26]. In [27], the effect of line parameters on microgrid stability is analyzed considering linear loads. Since the microgrid is located near the load location, the synchronous generators (SG) application seems difficult and infeasible for stability analysis. Hence it is relatively less worthy of accounting dynamics of SGs in microgrid [28]. In contrast, the majority of DGs in the microgrid are inverter-based; hence the mathematical model of microgrid consisting of power electronics-based sources has been widely utilized for stability analysis [29]. The load on a microgrid can be passive, active, and dynamic; hence various literature shows the stability analysis of microgrids with different loading

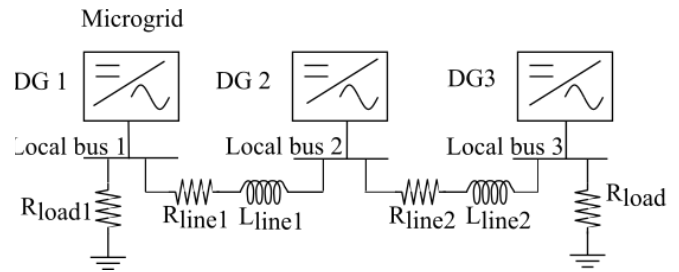


Fig. 1. Typical Structure of Voltage Source Inverter Coupled Microgrid

conditions [20, 30, 31]. The outcome of the active load parameter on the microgrid's stability is discussed in [17]. The negative resistance characteristic of constant power load may lead to the instability of a microgrid. In [32], the stability of the microgrid is explored considering constant power loads. The loading limit of the microgrid is obtained in this paper, but how the load parameters affect the system stability is not shown. In [18], the effect of induction motor (IM) load dynamics on medium-voltage microgrid stability is studied with a remote stabilization control scheme. Dynamic stability of an isolated microgrid considering direct online induction motor load is analyzed in [19] with a small-signal impedance model and Nyquist stability criterion. In [33], droop control is studied with linear and non-linear load employing time-domain simulation. The authors in [34] presents the effect of varying load on the small-signal model stability of an 11-bus microgrid system.

The state-space structure of microgrid is developed with certain assumptions, and stability study is carried out either with passive, active, and dynamic loads or a combination of different loads in literature. The objective of this work is to examine the impact of load dynamics on microgrid stability by building a comprehensive mathematical model of microgrid systems that includes passive, active, and dynamic loads. A detailed analysis of the system with time-domain simulations, eigenvalue analysis, and participation factor is presented.

The major contributions of the paper can be summarized as follows:

- 1) The comprehensive microgrid model with inverter interfaced DG, consisting of a power controller, a voltage and current controller, and an LCL filter is developed.
- 2) The passive load modeling is represented by R and RL load, RIAL is modeled considering control and filter dynamics of active load using the averaging method, and induction motor load is modeled in terms of stator and rotor dynamics.
- 3) Time-domain simulations and small-signal analysis are used to examine the system response under various loading conditions.

The remaining part of the paper is structured as follows: the state-space model of the system components is derived in Section 2. Section 3 presents the eigenvalue and participation factor analysis of the microgrid. In Section 4, the results and discussion from the simulation for various cases are presented. Section 5 concludes the work.

2. STATE-SPACE MODEL OF MICROGRID

Fig. 1 depicts a typical microgrid evaluated in this study. It has three voltage source inverters (VSI) interfaced DGs. The energy source's intermittent nature and the dynamics of the DC side are not taken into account. Each VSI interfaced DG is linked to load through LC filter and coupling inductor L_c . A common bus is connected with the respective DG source through line impedances R_{line} and L_{line} . When the isolation switch is in open condition microgrid is in autonomous mode.

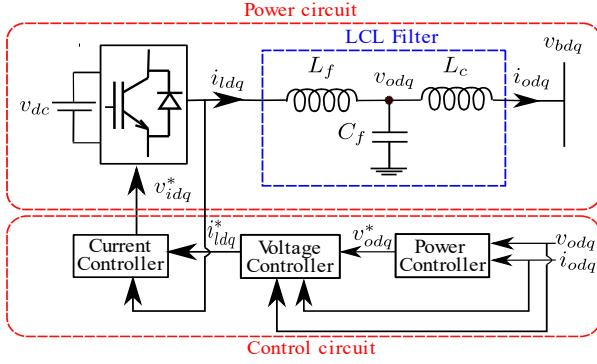


Fig. 2. Voltage source inverter DG block diagram

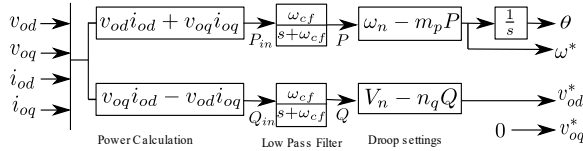


Fig. 3. Voltage source inverter DG block diagram

The stability of the microgrid is studied and analyzed in the form of non-linear mathematical equations. Hence these equations are linearized about an operating point to form a small-signal model and to examine the stability of the system. The small-signal dynamic model of the complete microgrid system is decoupled into three submodules.

- Parallel connected voltage source inverters DG sub-module.
- Network sub-module.
- Load sub-module.

First, the mathematical model of different submodules is derived and combined to yield the study system's complete model.

2.1. Modeling of a parallel-connected voltage source inverter DGs

In a microgrid, DGs are integrated into the system by VSI, LC filter, and coupling inductor, as illustrated in Fig. 1. The control circuit and power circuit of the DG are shown in Fig. 2. The power, current, and voltage controller form the control circuit. The switching bridge and LCL filter form the power circuit for the source system, as shown in Fig. 2.

A) Modeling of the power controller

The power controller resembles the governor of a conventional SG. Suppose load increases in an alternator, an increase in output power is fed by decreasing frequency. Similarly, in the inverter, any increase in load is manipulated by decreasing frequency based on the governor droop characteristic. The reactive power changes are compensated by changing voltage magnitude. The power controller is depicted in Fig. 3. Instantaneous real and reactive power (P_{in} and Q_{in}) are using measured output current (i_{od} and i_{oq}) and output voltage (v_{od} and v_{oq}) represented in dq reference frame by,

$$P_{in} = v_{od}i_{od} + v_{oq}i_{oq} \quad (1)$$

$$Q_{in} = v_{oq}i_{od} - v_{od}i_{oq}. \quad (2)$$

The instantaneous powers are processed through a low pass filter (LPF) with a cut-off frequency ω_{cf} to get average powers (P and Q) which are shown as,

$$P = \frac{\omega_{cf}}{s + \omega_{cf}} P_{in}, Q = \frac{\omega_{cf}}{s + \omega_{cf}} Q_{in} \quad (3)$$

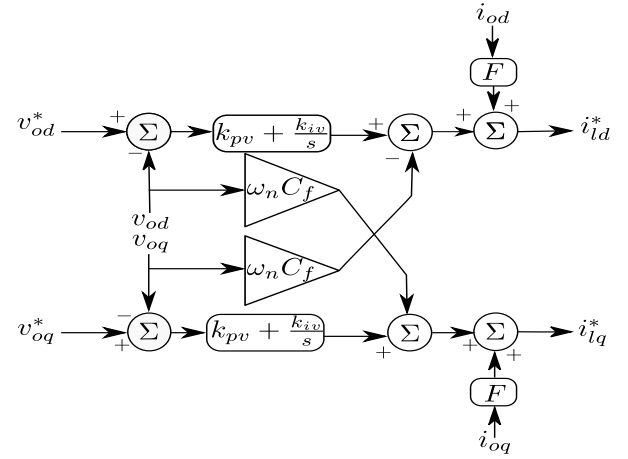


Fig. 4. Voltage controller

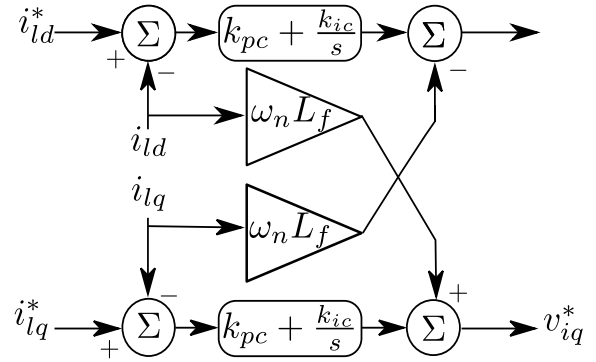


Fig. 5. Current controller

where s is the Laplace domain transform a factor. The fundamental voltage and frequency are set using droop gain given by,

$$\omega = \omega_n - m_p P, \quad (4)$$

$$v_{od}^* = v_{od,n} - n_q Q, v_{oq}^* = 0 \quad (5)$$

where m_p and n_q are static droop gains; ω_n and $v_{od,n}$ is nominal set point frequency and nominal set point voltage, respectively. All inverter parameters are converted from their respective reference frame to a common reference frame. The angle (δ_i) between the dq frame of the individual inverter and common DQ frame is defined as,

$$\delta_i = \int (\omega_i - \omega) dt \quad (6)$$

where, ω_i is the frequency of the respective inverter and ω is the common reference frame frequency.

B) Modeling of voltage controller

The voltage controller controls the output voltage using the PI controller, as shown in Fig. 4 [23].

The state equations of a controller are represented by,

$$\frac{d\phi_d}{dt} = v_{od}^* - v_{od}, \frac{d\phi_q}{dt} = v_{oq}^* - v_{oq}. \quad (7)$$

The algebraic equations for reference currents are shown as,

$$i_{id}^* = F i_{od} - \omega_n C_f v_{oq} + k_{pv} (v_{od}^* - v_{od}) + k_{iv} \phi_d \quad (8)$$

$$i_{iq}^* = F i_{oq} + \omega_n C_f v_{od} + k_{pv} (v_{oq}^* - v_{oq}) + k_{iv} \phi_q \quad (9)$$

where k_{pv} , k_{iv} are proportional and integral gains; F is the feed-forward term, and C_f is the filter's capacitance.

C) Modeling of the current controller

The current controller regulates the output inductor reference current using the PI controller, as displayed in Fig. 5.

The state equations of the current controller are represented by,

$$\frac{d\gamma_d}{dt} = i_{id}^* - i_{ld}, \quad \frac{d\gamma_q}{dt} = i_{iq}^* - i_{lq}. \quad (10)$$

The algebraic equations are

$$v_{id}^* = -\omega_n L_f i_{ld} + k_{pc}(i_{ld}^* - i_{ld}) + k_{ic}\gamma_d \quad (11)$$

$$v_{iq}^* = \omega_n L_f i_{lq} + k_{pc}(i_{iq}^* - i_{lq}) + k_{ic}\gamma_q \quad (12)$$

where k_{pc} , k_{ic} are proportional and integral gains, respectively, L_f is filter inductance, and i_{ld} , i_{lq} are filter inductor currents in dq reference frame.

D) Modeling of output LC filter and coupling inductor

It is considered that the inverter generates the required voltage ($v_i = v_i^*$), and switching losses are considered negligible. The state-space equations for output LC filter and coupling inductor are given by,

$$\frac{di_{ld}}{dt} = \frac{1}{L_f} (-r_f i_{ld} + v_{id} - v_{od}) + \omega i_{lq} \quad (13)$$

$$\frac{di_{lq}}{dt} = \frac{1}{L_f} (-r_f i_{lq} + v_{iq} - v_{oq}) - \omega i_{ld} \quad (14)$$

$$\frac{di_{od}}{dt} = \frac{1}{L_c} (-r_c i_{od} + v_{od} - v_{bd}) + \omega i_{oq} \quad (15)$$

$$\frac{di_{oq}}{dt} = \frac{1}{L_c} (-r_c i_{oq} + v_{oq} - v_{bq}) - \omega i_{od} \quad (16)$$

$$\frac{dv_{od}}{dt} = \omega v_{oq} + \frac{1}{C_f} (i_{ld} - i_{od}) \quad (17)$$

$$\frac{dv_{oq}}{dt} = -\omega v_{od} + \frac{1}{C_f} (i_{lq} - i_{oq}) \quad (18)$$

where r_f is the LC filter's internal resistance; r_c and L_c are coupling inductor's resistance and inductance, respectively; v_{bd} and v_{bq} are base voltages in dq reference frame.

E) Complete model of an individual inverter

The inverters are connected to the network by transforming the output variables of the inverter into a common reference frame. Hence the conversion of output current i_{odq} to i_{oDQ} is shown by,

$$\begin{bmatrix} i_D \\ i_Q \end{bmatrix}_{common} = \begin{bmatrix} \cos \theta & \sin \theta \\ -\sin \theta & \cos \theta \end{bmatrix} \begin{bmatrix} i_d \\ i_q \end{bmatrix}_{local}. \quad (19)$$

Similarly, input bus voltages to the inverters can be remodeled from a common reference frame to an individual reference frame by employing the reverse transformation given by,

$$\begin{bmatrix} v_d \\ v_q \end{bmatrix}_{local} = \begin{bmatrix} \cos \theta & -\sin \theta \\ \sin \theta & \cos \theta \end{bmatrix} \begin{bmatrix} v_D \\ v_Q \end{bmatrix}_{common} \quad (20)$$

The state-space model of an inverter is formed by interlinking power, current, and voltage control loops, an LC filter, and coupling inductor models. A state-space model of a single inverter unit in a common reference frame is represented by

$$\begin{aligned} \dot{[\Delta x_{INV}]} &= [A_{INV}] [\Delta x_{INV}] + [B_{INV}] [\Delta u_{bDQ}] \\ &+ [B_{\omega com}] [\Delta \omega_{com}] \end{aligned} \quad (21)$$

The individual inverter system contains a total of thirteen states, three inputs, and two outputs. The first inverter's frequency is considered as the reference frequency. Where A_{INV} is state matrix of i^{th} inverter, B_{INV} is the voltage input matrix, $B_{\omega com}$ is the

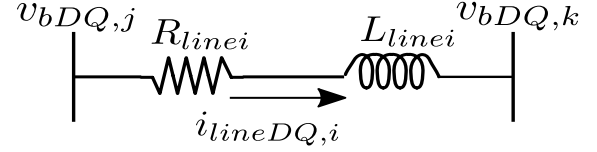


Fig. 6. Line model

input frequency matrix. $C_{INV \omega i}$ and $C_{INV c i}$ are output frequency and current matrices, respectively.

$$\begin{bmatrix} \Delta \omega_i \\ \Delta i_{oDQ i} \end{bmatrix} = \begin{bmatrix} C_{INV \omega i} \\ C_{INV c i} \end{bmatrix} [\Delta x_{INV i}] \quad (22)$$

where state vector $[x_{INV i}]$ of the inverter is $[\delta_i, P_i, Q_i, \phi_{dq i}, \gamma_{dq i}, i_{ld q i}, v_{od q i}]^T$.

F) Complete model of parallel-connected inverter DG system

In this paper, three inverters interfaced DGS are connected in parallel. All inverters are built using individual reference frame, and the complete model is formed using reference frame transformation.

The state-space representation of parallel-connected inverters can be represented by,

$$\begin{aligned} \dot{[\Delta X_{INV}]} &= [A_{INV}] [\Delta X_{INV}] + [B_{INV}] [\Delta v_{bDQ}] \\ &+ [B_{INV \omega}] [\Delta \omega_{com}] \end{aligned} \quad (23)$$

$$\begin{bmatrix} \Delta \omega_i \\ \Delta i_{oDQ i} \end{bmatrix} = \begin{bmatrix} C_{INV \omega} \\ C_{INV c} \end{bmatrix} [\Delta X_{INV}]. \quad (24)$$

Where A_{INV} is the state matrix of all the inverter submodules, B_{INV} and $B_{INV \omega}$ are input matrices of the complete inverter submodule related to the input voltage and frequency. $C_{INV c}$ is output matrices corresponding to the inverter output current.

In (23) and (24), for the "g" number of DG inverters state vector and output vector can be shown as,

$$[\Delta X_{INV}] = [\Delta x_{INV1}, \Delta x_{INV2}, \dots, \Delta x_{INVg}]^T \quad (25)$$

$$[\Delta Y_{INV}] = [\Delta i_{oDQ1}, \Delta i_{oDQ2}, \dots, \Delta i_{oDQg}]^T \quad (26)$$

2.2. Network model

The distribution line is represented as a network with resistance R_{line} and inductance L_{line} , as shown in Fig. 6. The dynamics of an i^{th} line connecting j^{th} source node and k^{th} load node given by,

$$\begin{aligned} \frac{di_{lineDi}}{dt} &= \frac{-R_{linei}}{L_{linei}} i_{lineDi} + \omega i_{lineQi} \\ &+ \frac{1}{L_{linei}} v_{bDj} - \frac{1}{L_{linei}} v_{bDk} \end{aligned} \quad (27)$$

$$\begin{aligned} \frac{di_{lineQi}}{dt} &= \frac{-R_{linei}}{L_{linei}} i_{lineQi} - \omega i_{lineDi} \\ &+ \frac{1}{L_{linei}} v_{bDj} - \frac{1}{L_{linei}} v_{bDk} \end{aligned} \quad (28)$$

The state-space representation for the network is given by,

$$\begin{aligned} \dot{[\Delta i_{lineDQ}]} &= [A_{LINE}] [\Delta i_{lineDQ}] + [B_{1LINE}] [\Delta v_{bDQ}] + \\ &[B_{2LINE}] [\Delta \omega_{com}]. \end{aligned} \quad (29)$$

Where A_{LINE} is the state matrix of the network submodule, and B_{1LINE} and B_{2LINE} are network submodules corresponding to the input voltage and reference frequency, respectively.

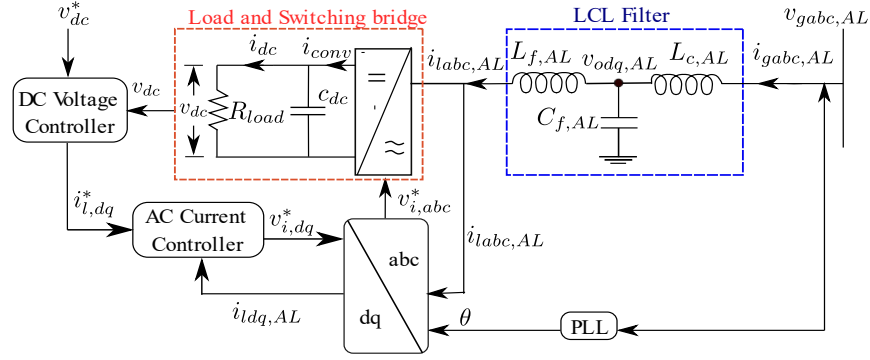


Fig. 7. Control circuit of RIAL

For l number of lines in (29), the line current vector is defined as,

$$[\Delta i_{lineDQ}] = [\Delta i_{lineDQ1}, \Delta i_{lineDQ2}, \dots, \Delta i_{lineDQl}]^T \quad (30)$$

$$[\Delta v_{bDQ}] = [\Delta v_{bDQ1}, \Delta v_{bDQ2}, \dots, \Delta v_{bDQm}]^T \quad (31)$$

2.3. Load model

In this paper, the stability of the islanded microgrid is explored, considering different loads connected to the node. Passive loads are modeled by a resistive or an inductive-resistive circuit. Active load is structured as constant power load or rectifier interfaced active load (RIAL). The IM is considered a dynamic load.

A) State-space model of a passive load

The R and RL type load can be expressed by given equations for the load allied at i^{th} node,

$$\frac{di_{loadDi}}{dt} = \frac{1}{L_{loadi}} (-R_{loadi}i_{loadDi} + v_{bDi}) + \omega i_{loadQi} \quad (32)$$

$$\frac{di_{loadQi}}{dt} = \frac{1}{L_{loadi}} (-R_{loadi}i_{loadQi} + v_{bQi}) - \omega i_{loadDi} \quad (33)$$

In general, for p passive loads, the state space representation for load is given by,

$$\begin{aligned} [\Delta \dot{X}_{PL}] &= [A_{PL}] [\Delta X_{PL}] + [B_{1PL}] [\Delta v_{bDQ}] \\ &+ [B_{2PL}] [\Delta \omega_{com}] \end{aligned} \quad (34)$$

where, A_{PL} is the state matrix of the passive load submodule, B_{1PL} and B_{2PL} are matrices related to the input voltage and reference frequency of the load submodule, respectively. In (34) the state vector $[\Delta X_{PL}]$ is defined as

$$[\Delta X_{PL}] = [\Delta i_{loadDQ1}, \Delta i_{loadDQ2}, \dots, \Delta i_{loadDQp}]^T \quad (35)$$

where is Δi_{loadDQ} load current at each node.

B) State-space model of a rectifier-interfaced active load

Fig. 7 shows the full control circuit for a RIAL. The DC voltage controller and AC current controller are shown in Fig. 8. The DC voltage controller regulated the voltage across the load by comparing it with a reference voltage.

The AC controller provides a reference voltage signal for the switching bridge of the load side inverter. The state-space equation for the DC voltage control circuit of the load is given by,

$$i_{id,AL}^* = k_{pv,AL}(v_{dc,AL}^* - v_{dc,AL}) + k_{iv,AL}\phi_{AL} \quad (36)$$

$$\frac{d\gamma_{dq,AL}}{dt} = i_{idq,AL}^* - i_{idq,AL} \quad (37)$$

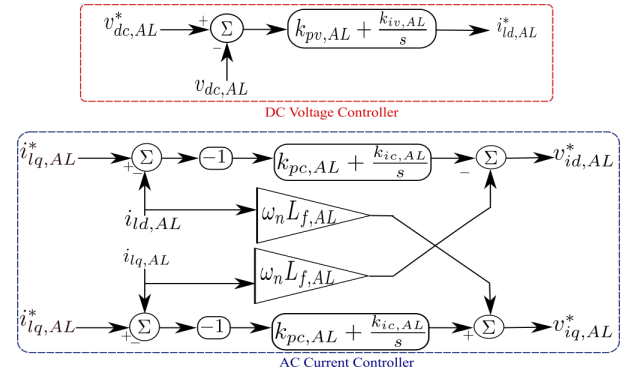


Fig. 8. Voltage and current control loop for RIAL [23]

where $k_{pv,AL}$ and $k_{iv,AL}$ is proportional and integral gains of DC voltage controller of RIAL respectively.

The state-space equation for AC current controller circuit is given by,

$$v_{id,AL}^* = \omega_n L_{f,AL} i_{id,AL} - k_{pc,AL}(i_{id,AL}^* - i_{id,AL}) - k_{ic,AL}\gamma_{d,AL} \quad (38)$$

$$v_{iq,AL}^* = -\omega_n L_{f,AL} i_{id,AL} - k_{pc,AL}(i_{iq,AL}^* - i_{iq,AL}) - k_{ic,AL}\gamma_{q,AL} \quad (39)$$

where $k_{pc,AL}$ and $k_{ic,AL}$ is proportional and integral gains of AC current controller of RIAL; $i_{d,AL}$ and $i_{q,AL}$ are inductor currents of LC filter of active load in dq reference frame. In general, the state space representation of RIAL used is shown as,

$$\begin{aligned} [\Delta \dot{X}_{AL}] &= A_{AL} [\Delta X_{AL}] + B_{1AL} [\Delta U_{AL}] \\ &+ B_{2AL} [\Delta v_{bDQ}] + B_{3AL} [\Delta \omega_{com}] \end{aligned} \quad (40)$$

where A_{AL} is the state matrix of the RIAL submodule, B_{1AL} , B_{2AL} , and B_{3AL} are matrices of RIAL submodule related to input control, input voltage, and reference frequency.

In (40) the state vector (ΔX_{AL}) and input vector (ΔU_{AL}) for RIAL is represented as,

$$[\Delta X_{AL}] = [\Delta \Phi_{AL}, \Delta \gamma_{dq,AL}, \Delta i_{idq,AL}, \Delta v_{odq,AL}, \Delta i_{gdq,AL}, \Delta v_{dc}]^T \quad (41)$$

$$[\Delta U_{AL}] = [\Delta v_{dc}^*, \Delta i_{idq,AL}^*, \Delta i_{dcdist}]^T \quad (42)$$

C) State-space model of an induction motor load

The currents of IM are taken as state variables for describing voltage equations [35]. Hence the IM can be represented in mathematical form using 5th order derivative model in the common DQ reference frame as

$$v_{Qs} = r_s i_{Qs} + L_{ss} \frac{di_{Qs}}{dt} + \omega L_{ss} i_{Ds} + L_m \frac{di_{Qr}}{dt} + \omega L_m i_{Dr} \quad (43)$$

Table 1. Low-frequency eigenvalues of the study system

Mode No.	Eigenvalues $\sigma \pm j\omega$	Damp. Ratio ζ	Damp. Freq. f_d (Hz)
1, 2	-129.84±206.7i	0.531	32.9
3,4	-71.8±147i	0.436	23.5
5	-125.7	1	0
6	-57.7	1	0
7	-9.2	1	0
8,9	-13.99±20.03i	0.5728	3.18
10	-32.031	1	0
11,12	-31.37±0.061i	0.99	0.009

$$v_{Ds} = -\omega L_{ss} i_{Qs} + r_s i_{Ds} + L_{ss} \frac{di_{Ds}}{dt} - \omega L_m i_{Qr} + L_m \frac{di_{Dr}}{dt} \quad (44)$$

$$v_{Qr} = L_m \frac{di_{Qs}}{dt} + s \omega L_m i_{Ds} + r_r i_{Qr} + L_{rr} \frac{di_{Qr}}{dt} + s \omega L_{rr} i_{Dr} \quad (45)$$

$$v_{Dr} = -s \omega L_m i_{Qs} + L_m \frac{di_{Ds}}{dt} - s \omega L_{rr} i_{Qr} + r_r i_{Dr} + L_{rr} \frac{di_{Dr}}{dt} \quad (46)$$

where r_s and r_r are resistances of stator and rotor windings, respectively; L_{ss} and L_{rr} are inductance of stator and rotor windings, respectively; L_m is mutual inductance; s and ω are rotor slip and supply frequency of stator, respectively. The relation between electromagnetic torque, stator, and rotor currents can be stated as,

$$T_e = \frac{3}{2} \left(\frac{P_{IM}}{2} \right) L_m (i_{Qs} i_{Dr} - i_{Ds} i_{Qr}) \quad (47)$$

The correlation between electromagnetic torque (T_e) and load torque (T_L) can be deduced in terms of the slip (s) and angular synchronous speed (ω_s) as,

$$T_e - T_L = J \frac{d}{dt} ((1-s) \omega_s) \quad (48)$$

In (47) and (48), P_{IM} is number of poles, J is total motor and load inertia and T_L is load torque. By using (43)–(48), the complete state-space representation of the induction motor load is obtained as,

$$\begin{aligned} \Delta \dot{X}_{IM} &= [A_{IM}] \Delta X_{IM} + [B_{1IM}] \Delta U_{IM} \\ &+ [B_{2IM}] \Delta \omega + [B_{3IM}] \dot{\Delta \omega} \end{aligned} \quad (49)$$

where A_{IM} is the state matrix of load submodule, B_{1IM} , B_{2IM} and B_{3IM} are load submodule matrices related to voltage, and frequency. In (49),

$$\Delta X_{IM} = [\Delta i_{Qs}, \Delta i_{Ds}, \Delta i_{Qr}, \Delta i_{Dr}, \Delta s_i]^T \quad (50)$$

$$\Delta U_{IM} = [\Delta v_{Qs}, \Delta v_{Ds}, \Delta v_{Qr}, \Delta v_{Dr}, \Delta T_L]^T \quad (51)$$

2.4. State-space representation of complete microgrid

The microgrid's comprehensive state-space model is derived from the relationship between the system's input and output. The input variables in the microgrid are node voltages, and the output variables are DG output currents. To eliminate switching harmonics, LCL filters are connected between the switching bridge and the grid. However, the closed-loop system could be

Table 2. Eigenvalues introduced and affected by RIAL in the study system

Mode No.	Eigenvalues $\sigma \pm j\omega$	Damp. Ratio ζ	Damp. Freq. f_d (Hz)
1, 2	-4343471±314.1i	1	50
3,4	-1180.3±123123i	0.095	1959
5,6	-1254.8±11770i	0.106	1873
7,8	-3137.2±5066.7i	0.526	806
9,10	-2926.8±4594.4i	0.537	731
11,12	-3306.2±3282.6i	0.709	22.4
13,14	-2783.1±2869.3i	0.69	456.66
15,16	-1019.4±2308.8i	0.403	367.4
17,18	-1054.9±2186.9i	0.434	348.07
19,20	-1785.8±1644.3i	0.735	261.71
21,22	-1704.3±1509.3i	0.748	240.21
23,24	-1373.1±1790.2i	0.6	284.9
25,26	-47.7±165.0i	0.277	26.27

destabilized by LCL filter resonance and high grid side impedance. The common bus voltages can be shown as,

$$v_{bDi} = r_v (i_{oDi} - i_{loadDi} + i_{lineDi,j}) \quad (52)$$

$$v_{bQi} = r_v (i_{oQi} - i_{loadQi} + i_{lineQi,j}) \quad (53)$$

where r_v is the resistance of the virtual resistor. In general, for the n node system, the small-signal model is represented as,

$$\begin{aligned} [\Delta v_{bDQ}] &= R_v (M_{INV} [\Delta i_{oDQ}] + M_{LOAD} [i_{loadDQ}]) \\ &+ M_{LINE} [\Delta i_{lineDQ}]. \end{aligned} \quad (54)$$

where R_v is a diagonal matrix of r_v of size $n \times n$, M_{INV} represents the mapping of nodes and inverter sub-module of size $2n \times 2g$, M_{LOAD} represents the mapping of nodes and load of size $2n \times 2p$, M_{LINE} represents the mapping of nodes and network sub-module of size $2n \times 2l$.

The elements of mapping matrices M_{INV} , M_{LOAD} , and M_{LINE} are further expressed as,

$$M_{INV}(i, j) = \begin{cases} 1, & \text{if } j^{\text{th}} \text{ is linked to } i^{\text{th}} \text{ node,} \\ 0, & \text{if } j^{\text{th}} \text{ is not linked to } i^{\text{th}} \text{ node.} \end{cases}$$

$$M_{LINE}(i, j) = \begin{cases} -1, & \text{if } j^{\text{th}} \text{ line is linked to } i^{\text{th}} \text{ node and} \\ & \text{current is flowing away from node,} \\ 1, & \text{if } j^{\text{th}} \text{ line is linked to } i^{\text{th}} \text{ node} \\ & \text{and current is flowing towards node.} \end{cases}$$

$$M_{LOAD}(i, j) = \begin{cases} -1, & \text{if } j^{\text{th}} \text{ passive, active or dynamic} \\ & \text{load stator is linked to } i^{\text{th}} \text{ node,} \\ 0, & \text{There is no load associated to the node.} \end{cases}$$

$$\begin{bmatrix} \Delta X_{INV} \\ \Delta X_{LINE} \\ \Delta X_{LOAD} \end{bmatrix} = A_{sys} \begin{bmatrix} \Delta X_{INV} \\ \Delta X_{LINE} \\ \Delta X_{LOAD} \end{bmatrix} \quad (55)$$

where A_{sys} represents a state-space matrix of microgrid, X_{INV} , X_{LOAD} , and X_{LINE} are state variable matrix of inverter submodule, network submodule, and load submodule, respectively.

The microgrid inverter parameters, RIAL parameters, and IM parameters are given in Appendix.

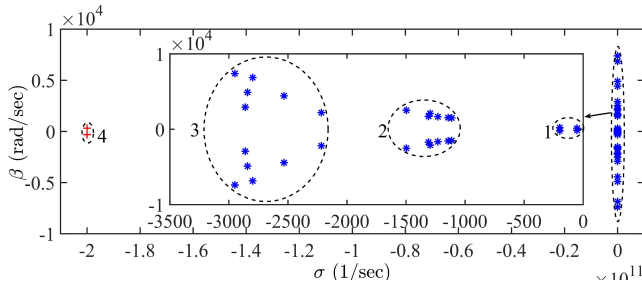


Fig. 9. Eigenvalue plot of microgrid with RL load

3. SMALL-SIGNAL ANALYSIS

The state-space model of a microgrid developed in Section 2 is used to analyze the stability of the microgrid while considering the various loading conditions. The eigenvalue analysis, and time-domain simulation of three inverter source systems operating at 220 V, 50 Hz are shown for different cases considering passive, active, and induction motor load.

The eigenvalues are modes of the system which give insights into the stability of the system through the oscillation frequency and magnitude of the damping ratio. The (55) yields the complete state-space model of the system, and the matrix A_{sys} is a system matrix that includes network and load parameters. The participation factor indicates which state is active for a given eigenvalue. They highlight the states responsible for the low-frequency dominant mode. Participation factors are determined by

$$P_{ki} = \phi_{ki}\psi_{ik} \quad (56)$$

where, ϕ_{ki} is the k^{th} element in the right eigenvector ϕ_i , and ψ_{ik} is the k^{th} element in the left eigenvector ψ_i corresponding to the eigenvalue λ_i [36]. k shows the state variable number for which the participation factor is evaluated.

3.1. Passive load connected to the microgrid

The eigenvalue plot of the microgrid with RL load is shown in Fig. 9. The entire eigenvalue spectrum is split into four regions (each region is marked by dashed circle). The dominant low-frequency modes are displayed in Table 1. There are ten eigenvalues in Region-1, including four complex pairs with low frequency and damping ratio around 0.43-0.53 (Mode No.1,2,3,4,8,9,11,12). The participation plot shown in Fig. 10 confirms that the states of the droop controller and power controller are dominant in low-frequency eigenvalue in Region-1. Region-2 contains six complex pairs of eigenvalues with frequencies in the range from 200 Hz to 350 Hz with a low damping ratio of 0.5-0.6. The states of the current and voltage control loop are dominant factors for these modes. Region-3 contains six high-frequency eigenvalues because of the LCL filter and line state variables. Region-4 contains four complex pairs of eigenvalues. One pair due to passive load state variables is shown in Fig. 9. Since low-frequency modes are related to power controllers, they are insensitive to the dynamics of passive load.

3.2. Active load connected to the microgrid

Table 2 shows the eigenvalue introduced and affected by state variables of RIAL. Fig. 11 and Fig. 12 depict the eigenvalue plot and participation plot, respectively, for microgrid connected with RIAL. The complete eigenvalue spectrum is split into five regions. It is clear from Fig. 11 that load introduces a complex pair of eigenvalues (Mode No.25, 26) with a frequency of 26 Hz and damping ratio of 0.27 in Region-1. The capacitor voltage v_{dc} and voltage controller at the DC side (see Fig. 8) are dominant states for this mode. Two complex pairs of eigenvalues (Mode No.3,4,5,6) with a frequency of around 2 kHz and damping ratio

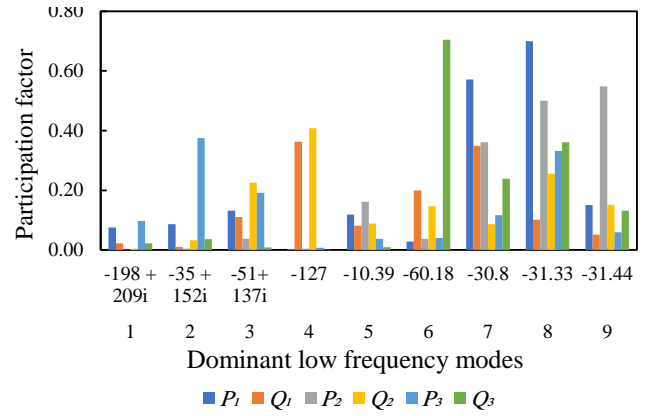


Fig. 10. Participation plot of power controller variables in low-frequency modes

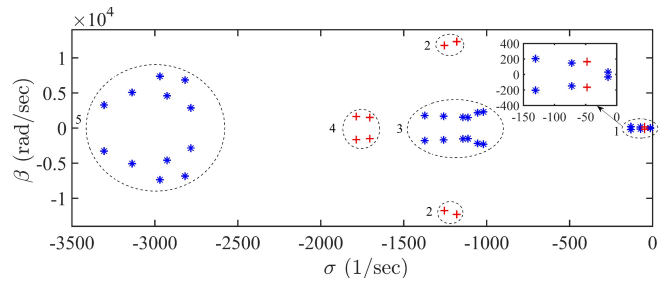


Fig. 11. Eigenvalue plot of microgrid with active load

of nearly 0.1 located in Region-2 are related to the AC side LCL Filter.

In Region-3, two eigenvalues with a frequency range of 250 Hz-300 Hz and a damping ratio in the range 0.6–0.7 (Mode No.19,20,21,22) appear. It is observed that, the affecting states in this mode are related to the current controller and coupling inductor.

3.3. Induction motor connected to the microgrid

The microgrid system’s eigenvalue plot with IM load is shown in Fig. 13. The entire eigenvalue spectrum is split into three regions. The coupling of IM with microgrid induces prominent oscillations in real power, reactive power, voltage, and frequency; as a result, two less damped complex pairs and the null point are introduced. The poorly damped mode is most affected by the d -axis stator and q -axis rotor current, as shown in Fig. 14.

4. TIME-DOMAIN ANALYSIS

In this section, time-domain results are discussed by applying a step change in load power for different types of loads to examine the stability of the microgrid.

4.1. Simulation results of microgrid with passive load

The study system has an initial load of 5.8 kW (25 Ω per phase) at Local bus 1 and 7.3 kW (20 Ω per phase) at Local bus 3. The low-frequency mode of the system is excited by a step increase of 3.9 kW in real power applied at $t=0.8$ seconds at Local bus 1.

Fig. 15(a) shows that initially, DG1 compensates for the major change in real power, as it is located near to load together with DG2 and DG3 responds slowly. In a steady-state, the load is shared equally by all DGs. Fig. 15(b) depicts that reactive power-sharing is unequal. Fig. 15(c) represents the drop in frequency due to an increase in load. All the DGs share load equally, and frequency is

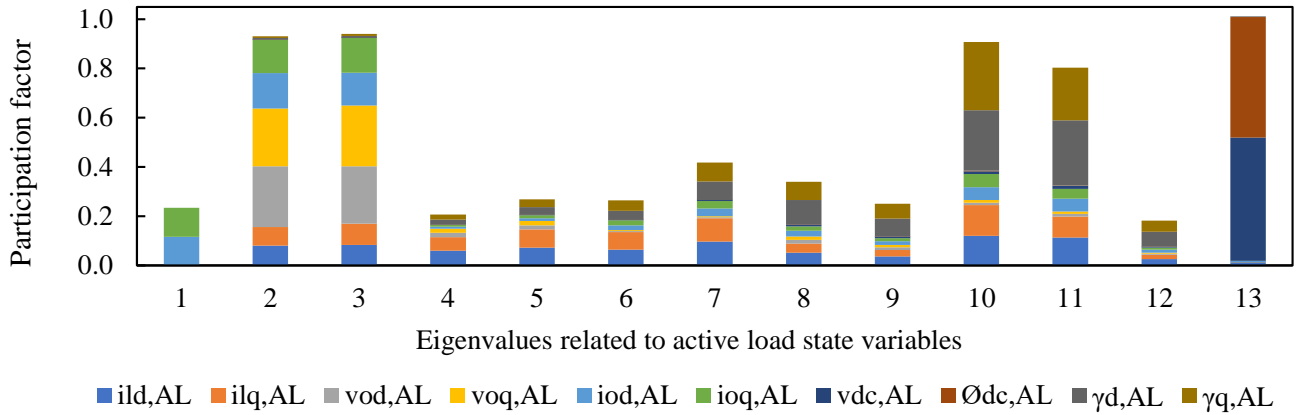


Fig. 12. Participation analysis of active load state variables in microgrid

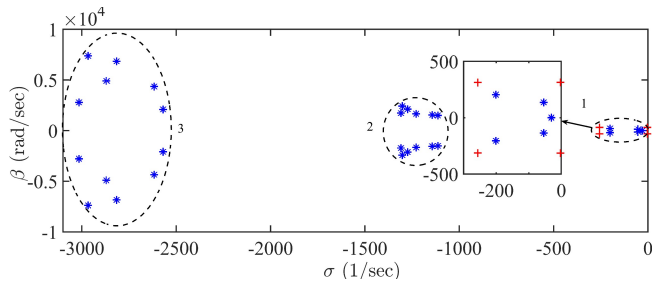


Fig. 13. Eigenvalue plot of the system with induction motor load

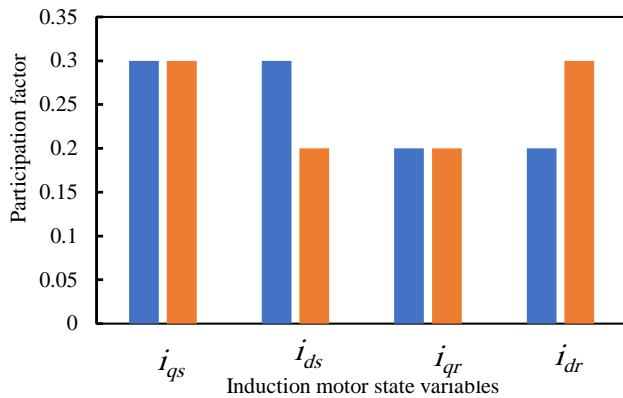
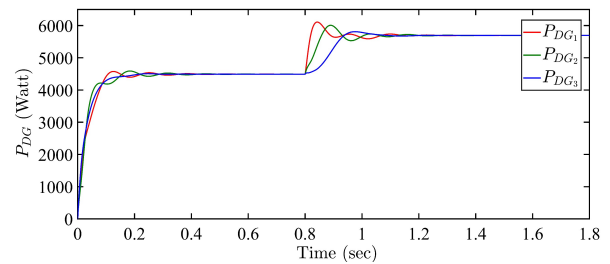


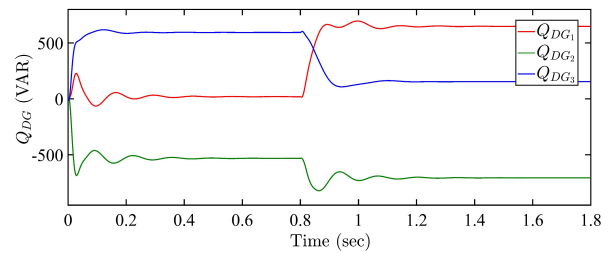
Fig. 14. Participation analysis of induction motor state variables in microgrid

set to a new value based on droop characteristics. The high value of droop gain can make power-sharing better among the DGs, but the oscillations in frequency may appear, which can affect the system's stability and voltage regulation.

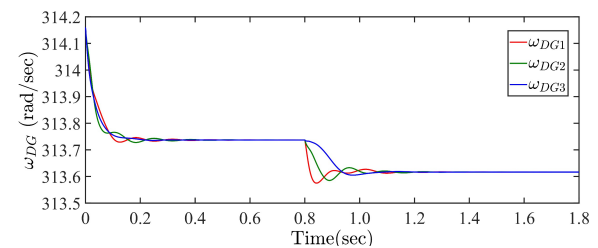
In Fig. 16, as the load on Local bus 1, is increased at 0.8 sec (see i_{load1} in Fig. 16(a)), the DG1 responds quickly (see i_{odDG1} in Fig. 16(b)). In the transient period after the switching event, the output current of DG1 is observed with peak overshoot. A similar change is observed in the response of line currents (see i_{lined1} Fig. 16(c)). Due to the same droop gain of all the DGs, the DGs share the change in load applied at Local bus 1 evenly after the transient phase. As a result, since the RL branches are used to distribute the compensating powers from the DGs, the line current responses are also impacted. The line current direction is assumed



(a)



(b)



(c)

Fig. 15. Dynamic responses of DGs with 3.9 kW of a step-change in load power at Local bus 1: (a) Real Power P_{DG} , (b) Reactive Power Q_{DG} , (c) frequency of DG units

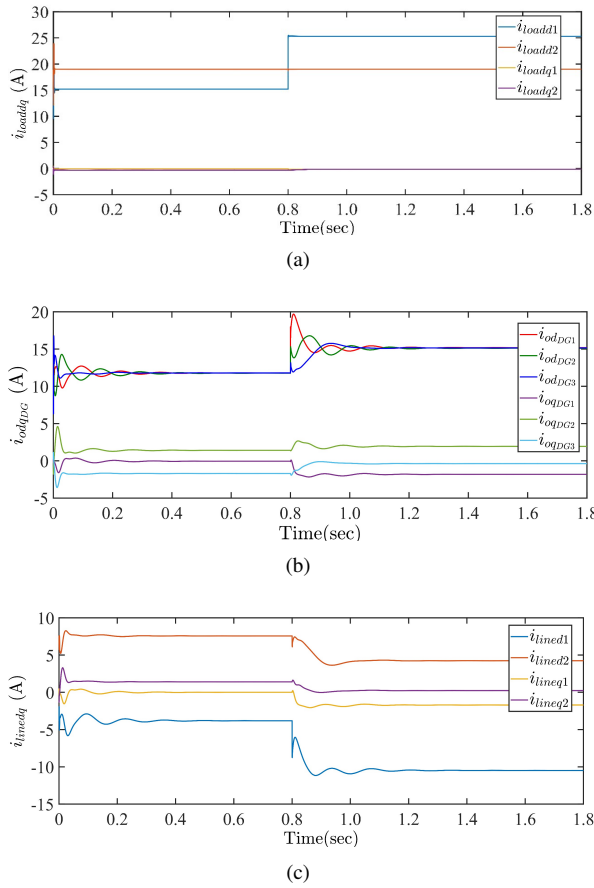


Fig. 16. Dynamic responses of microgrid with 3.9 kW of a step-change in load power at Local bus 1: (a) load currents i_{loaddq} , (b) DGs output current i_{odqDG} , (c) line currents i_{linedq}

to be positive when the current flows away from the node and negative when the current flows towards the node.

The high-frequency modes are examined by a sudden change of R load from 0 to 28 kW at Local node 1. Fig. 17(a) and 17(b) show the output voltage and d-axis inductor current of all the DGs, respectively. The notch (of $(381 - 307/381) * 100 = 19.42\%$) for less than 1 msec is observed in the output voltage waveform of inverter 1, which is connected near to the load point. High-frequency modes are most affected by the load condition of the microgrid.

Fig. 18 shows the system's simulation results when the RL load is increased to 16.9 kW and 13 kVAR from 0 at node 1. Initially, transients are observed in the output of DG1; then, gradually, all inverters share power equally. The results show that the change in reactive power is inappropriate. However, the high value of droop gain can ameliorate reactive power-sharing, but it adversely affects voltage regulation. The load change has an insignificant effect on low-frequency modes in the microgrid.

4.2. Simulation results of microgrid with active load

In this case, a passive R load of 6.9 kW (21 Ω per phase) and RIAL of 7.3 kW is connected to Local bus 1 and Local bus 3 respectively. The sudden step increase of 3.6 kW in DC load is applied at $t=0.5$ second to espy the low-frequency modes of the inverters and active load. According to participation analysis results, there is no correlation between the low-frequency modes of the inverters and the active load. As the inverter droop controllers swing against each other, the fundamental inverter power-sharing is seen in Fig. 19(a) and 19(b). Fig. 19(c) shows DC voltage output when the active load is increased by 3.6 kW.

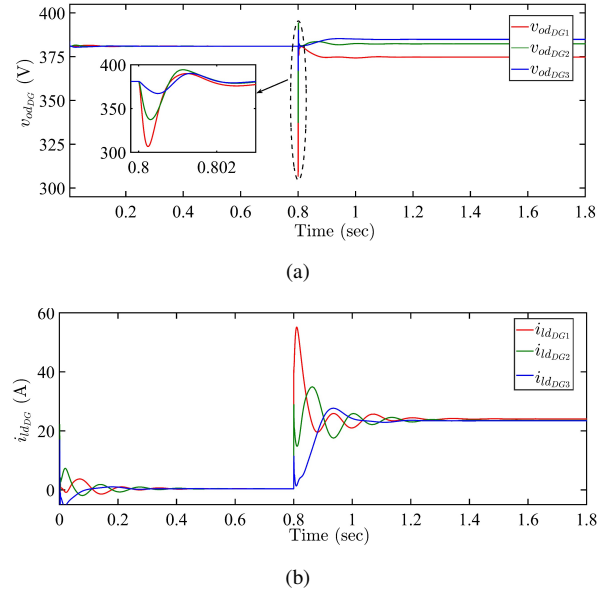


Fig. 17. Dynamic responses of the system when the load is changed suddenly from no load to 28 kW: (a) variation in d-axis output voltage v_{odDG} , (b) variation in d-axis inductor current i_{idDG}

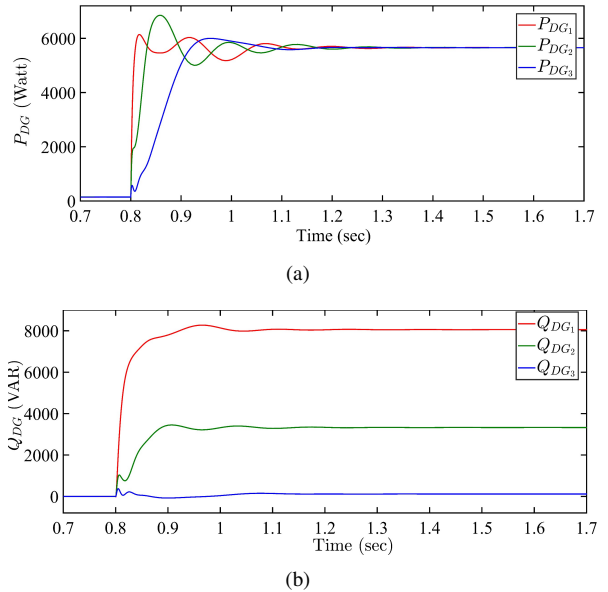


Fig. 18. Dynamic responses of DGs with a sudden change in RL load from no load to 16.9 kW and 13 kVAR at Local bus 1: (a) Real Power P_{DG} , (b) Reactive Power Q_{DG}

4.3. Simulation results of microgrid with induction motor load.

Fig. 20(a) and 20(b) respectively show DG's real power and reactive power responses when IM load is applied. The real power response, as can be seen, exhibits oscillatory behavior due to low-frequency modes introduced by IM.

Fig. 21(a) and 21(b) show rotor speed of IM and frequencies of all DG units respectively. The oscillations in speed are reflected in the output frequency of DG units, which in turn affects the input power of the IM through the droop controller.

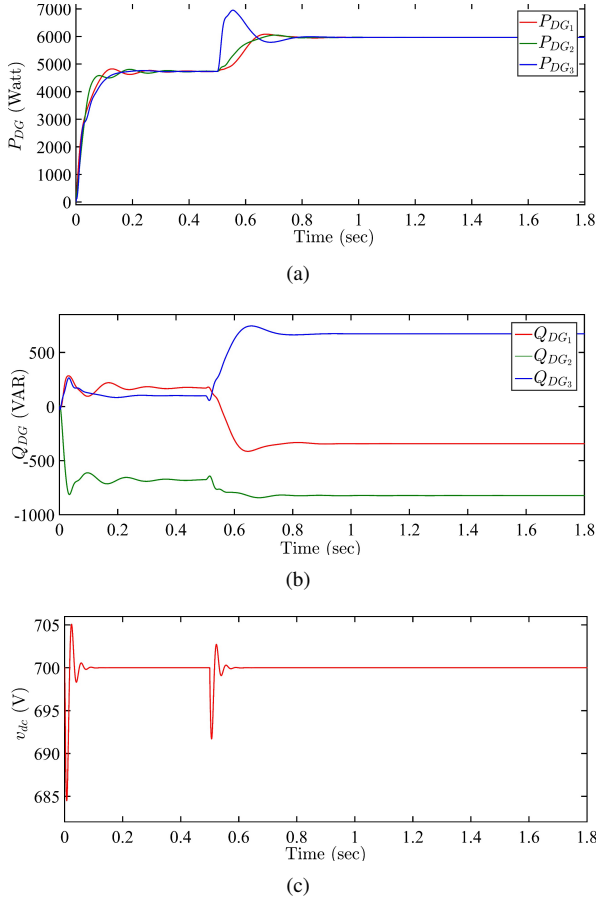


Fig. 19. Dynamic responses of DGs with step change of 3.6 kW in RIAL at Local bus 1: (a) Real Power P_{DG} , (b) Reactive Power Q_{DG} , (c) DC link capacitor voltage v_{dc} in RIAL

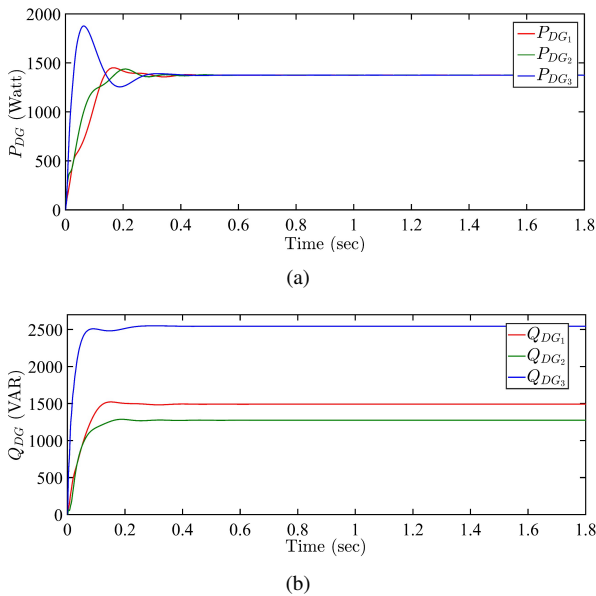


Fig. 20. Dynamic response of DG units when IM load is applied: (a) Real power P_{DG} , (b) Reactive power Q_{DG} .

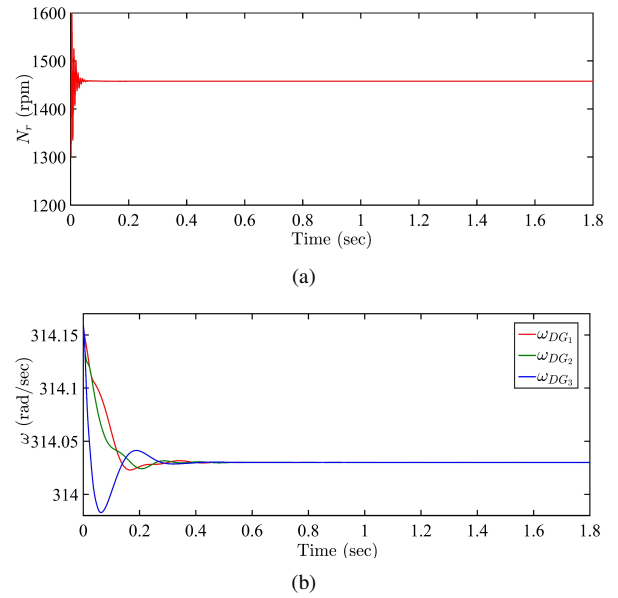


Fig. 21. Dynamic response of DG units when IM load is applied: (a) Rotor speed N_r , (b) Output frequency ω of DG units.

5. CONCLUSION

This paper presents a detailed stability analysis of microgrids using a small-signal model with time-domain simulations. The state-space model of the microgrid with different loading is developed to see the effect of load dynamics on the system's stability. The microgrid state-space model is designed for various instances, including passive load, rectifier-controlled active load, and dynamic load. The stability of a system is examined by eigenvalue analysis, and it is supported by time-domain simulations. The participation analysis is utilized to examine the participation of dominant states in various modes. The results reveal that when a microgrid is subjected to a step increase in RIAL, low-frequency oscillations are introduced by the DC voltage controller, and AC current controller influences the system's stability. In contrast, sudden high change in passive load causes appearance of high frequency modes. The sudden small change in passive load affects the power-sharing of DGs in transient periods and causes low-frequency oscillations. The time-domain results show that IM load induces oscillations momentarily in the dynamic response of the microgrid. The IM load introduces lightly damped eigenvalues which provoke rotor electromechanical oscillations. The effect of these modes is also reflected in the active power and frequency response of the microgrid. The time-domain results shown in this paper corroborate the eigenvalue analysis.

APPENDIX

Table A.1. Inverter Parameters [23]

f_s	8 kHz	m_p	9.4×10^{-5}
L_f	1.35 mH	n_q	1.3×10^{-3}
C_f	50 F	k_{pv}	0.05
r_f	0.1 Ω	k_{iv}	390
L_c	0.35 mH	k_{pc}	10.5
r_{Lc}	0.03 Ω	k_{ic}	16×10^3
ω_c	31.41 rad/sec	F	0.75

Table A.2. Active Load Parameters [17]

f_{sw}	10,000 Hz	c_{dc}	2040 F
L_f	2.3 mH	R_{load}	84.5 Ω
C_f	8.8 F	k_{pv}	0.5
r_f	0.1 Ω	k_{iv}	125
L_c	0.93 mH	k_{pc}	15
r_{Lc}	0.03 Ω	k_{ic}	25×10^3

Table A.3. Induction motor Parameters, 10 Hp, 400 V [20]

f_s	50 Hz	r_s	0.7834 Ω
L_{ss}	127.1 mH	r_r	0.7402 Ω
L_{rr}	127.1 mH	L_{rr}	124.1 mH
P_{IM}	4	T_L	47.75 N.m

REFERENCES

- [1] R.Ghanizadeh, M.Ebadian, and G B. Gharehpetian. "Control of inverter-interfaced distributed generation units for voltage and current harmonics compensation in grid-connected microgrids." *J. Oper. Autom. Power Eng.* vol. 4, no. 1, pp. 66–82, 2016.
- [2] P. Shah and B. Mehta, "Mitigation of grid connected distributed solar photovoltaic fluctuations using battery energy storage station and microgrid," *Inter. J. Power Energy Convers.*, vol. 12, no. 2, p. 153, 2021.
- [3] G. Shahgholian, "A brief review on microgrids: Operation, applications, modeling, and control," *Inter. Trans. Electri. Energy Syst.*, vol. 31, no. 6, 2021.
- [4] H. Radmanesh, M. Saeidi. "Stabilizing Microgrid Frequency by Linear Controller Design to Increase Dynamic Response of Diesel Generator Frequency Control Loop". *J. Oper. Autom. Power Eng.*, vol. 7, no. 2, pp. 216-226, 2019.
- [5] A. Jasemi, H. Abdi. "Probabilistic Multi-Objective Optimal Power Flow in an AC/DC Hybrid Microgrid Considering Emission Cost," *J. Oper. Automa. Power Eng.*, vol. 10, no. 1, pp. 13–27, 2022.
- [6] A. Khorshidi, T. Niknam, and B. Bahmani. "Synchronization of microgrid considering the dynamics of V2Gs using an optimized fractional order controller-based scheme." *J. Oper. Automa. Power Eng.* vol. 9, no. 1, pp. 11–22, 2021.
- [7] E. Naderi, A. Dejamkhooy, S.J. SeyedShenava, H. Shayeghi, "MILP based Optimal Design of Hybrid Microgrid by Considering Statistical wind Estimation and Demand Response," *J. Oper. Automa. Power Eng.*, vol. 10, no. 1, pp. 54-65, 2022.
- [8] M. Ahmed, L. Meegahapola, A. Vahidnia and M. Datta, "Stability and Control Aspects of Microgrid Architectures—A Comprehensive Review," *IEEE Access*, vol. 8, pp. 144730-144766, 2020.
- [9] Guerrero, J. Vasquez, J. Matas, L. de Vicuna and M. Castilla, "Hierarchical Control of Droop-Controlled AC and DC Microgrids—A General Approach Toward Standardization," *IEEE Trans. Ind. Electron.*, vol. 58, no. 1, pp. 158-172, 2011.
- [10] J. P. Lopes, C. L. Moreira, and A. Madureira, "Defining control strategies for microgrids islanded operation," *IEEE Trans. power syst.*, vol. 21, no. 2, pp. 916–924, 2006.
- [11] A. Singh and S. Parida, "Need of distributed generation for sustainable development in coming future," *IEEE Inter. Conf. Power Electron. Drives Energy Syst. (PEDES)*, pp. 1–6, 2012.
- [12] N. Gupta and P. Paliwal, "Novel droop integrated technique for regulation of islanded and grid-connected hybrid microgrid," *Inter. J. Power Energy Convers.*, vol. 12, no. 2, p. 89, 2021.
- [13] A. Samarat, B. MEHTA, S. Joshi. "Analysis and Modeling of AC and DC Micro-Grids for Prosumer Based Implementation," *J. Oper. Autom. Power Engineering*, vol. 9, no. 2, pp. 116-122, 2021.
- [14] M. Kazeminejad, M. Banejad, U. Annakkage, N. Hosseinzadeh. "The Effect of High Penetration Level of Distributed Generation Sources on Voltage Stability Analysis in Unbalanced Distribution Systems Considering Load Model," *J. Oper. Autom. Power Eng.*, 7, 2, 2019, 196-205.
- [15] M. H. Roos, P. H. Nguyen, J. Morren and J. G. Sloopweg, "Stability Analysis of Microgrid Islanding Transients Based on Interconnected Dissipative Subsystems," *IEEE Trans. Smart Grid*, vol. 12, no. 6, pp. 4655-4667, Nov. 2021.
- [16] Shuai, Z., Sun, Y., Shen, Z., Tian, W., Tu, C., Li, Y. and Yin, X., 2016. *Microgrid stability: Classification and a review. Renewable and Sustainable Energy Reviews*, 58, pp. 167-179.
- [17] N. Bottrell, M. Prodanovic, and T. C. Green, "Dynamic stability of a microgrid with an active load," *IEEE Trans. power electron.*, vol. 28, no. 11, pp. 5107–5119, 2013.
- [18] A. Kahrobaeian and Y. A.-R. I. Mohamed, "Analysis and mitigation of low-frequency instabilities in autonomous medium-voltage converter based microgrids with dynamic loads," *IEEE Trans. Ind. Electron.*, vol. 61, no. 4, pp. 1643–1658, 2013.
- [19] A. A. A. Radwan and Y. A.-R. I. Mohamed, "Analysis and active impedance-based stabilization of voltage-source-rectifier loads in grid connected and isolated microgrid applications," *EEE Trans. Sustainable Energy*, vol. 4, no. 3, pp. 563–576, 2013.
- [20] P. Raju and T. Jain, "Development and validation of a generalized modeling approach for islanded inverter-based microgrids with static and dynamic loads," *Int. J. Electr. Power Energy Syst.*, vol. 108, pp. 177–190, 2019.
- [21] Majumder, R., 2010. Modeling, stability analysis and control of microgrid, Ph.D., *Queensland University of Technology*.
- [22] J. Ma, X. Wang and X. Lan, "Small-Signal Stability Analysis of Microgrid Based on Perturbation Theory," *Asia-Pacific Power Energy Eng. Conf.*, 2012, pp. 1-4,
- [23] N. Pogaku, M. Prodanovic, and T. C. Green, "Modeling, analysis and testing of autonomous operation of an inverter-based microgrid," *IEEE Trans. power electron.*, vol. 22, no. 2, pp. 613–625, 2007.
- [24] M. Rasheduzzaman, J. A. Mueller, and J. W. Kimball, "An accurate small-signal model of inverter-dominated islanded microgrids using dq reference frame," *IEEE J. Emerging Sel. Top. Power Electron.*, vol. 2, no. 4, pp. 1070–1080, 2014.
- [25] A. U. Krismanto and N. Mithulananthan, "Identification of modal interaction and small signal stability in autonomous microgrid operation," *IET Gener. Transm. Distrib.*, vol. 12, no. 1, pp. 247– 257, 2017.
- [26] R. M. Kamel, A. Chaouachi, K. Nagasaka, "Detailed analysis of micro-grid stability during islanding mode under different load conditions," *Engineering*, vol. 3, no. 5, p. 508, 2011.
- [27] S. Tabatabaee, H. R. Karshenas, A. Bakhshai, and P. Jain, "Investigation of droop characteristics and x/r ratio on small-signal stability of autonomous microgrid," *IEEE 2nd Power Electron. Drive Syst. Techno. Conf.*, 2011, pp. 223–228.
- [28] D. K. Dheer, N. Soni, and S. Doolla, "Improvement of small signal stability margin and transient response in inverter-dominated microgrids," *Sustainable Energy Grids Networks*, vol. 5, pp. 135–147, 2016.
- [29] F. Katiraei, M. Iravani, and P. Lehn, "Small-signal dynamic model of a micro-grid including conventional and electronically interfaced distributed resources," *IET Gener. Transm. Distrib.*, vol. 1, no. 3, pp. 369–378, 2007.
- [30] S. Rezaee, M. Moallem, J. Wang, and A. A. A. Radwan, "Assessment of dynamic instabilities in weak grids with high penetration of power electronic loads," *IEEE 8th Intern. Conf. Smart Energy Grid Eng. (SEGE)*, 2020, pp. 13–17.
- [31] E.S.N. Raju P, T. Jain, "Impact of load dynamics and

- load sharing among distributed generations on stability and dynamic performance of islanded ac microgrids," *Electr. Power Syst. Res.*, vol. 157, pp. 200–210, 2018.
- [32] D. P. Ariyasinghe and D. M. Vilathgamuwa, "Stability analysis of microgrids with constant power loads," pp. 279–284, 2008.
- [33] A. Khaledian and M. Aliakbar Golkar, "Analysis of droop control method in an autonomous microgrid," *J. Appl. Res. Technol.*, vol. 15, no. 4, pp. 371–377, 2017.
- [34] F. D. Mohammadi, H. K. Vanashi, and A. Feliachi, "State-space modeling, analysis, and distributed secondary frequency control of isolated microgrids," *IEEE Trans. Energy Convers.*, vol. 33, no. 1, pp. 155–165, 2017.
- [35] P. Krause, O. Wasynczuk, S. Sudhoff and S. Pekarek, Analysis of electric machinery and drive systems. John Wiley & Sons, 2013.
- [36] K. Padiyar, *Power system dynamics: stability & control*, BS publications, 2010.